The Astrophysical Journal, 1003:11 (12pp), 2026 May 20 https://doi.org/10.3847/1538-4357/ae5a27


# X-Ray and Radio Campaign of the Z-source GX 340+0. II. The X-Ray Polarization in the Normal Branch

Yash Bhargava[1,2], Thomas D. Russell[3], Mason Ng[4,5], Arvind Balasubramanian[6], Liang Zhang[7], Swati Ravi[8], Vishal Jadoliya[9], Sudip Bhattacharyya[1], Mayukh Pahari[9], Jeroen Homan[10], Herman L. Marshall[8], Deepto Chakrabarty[8], Francesco Carotenuto[11,12], and Aman Kaushik[1]

[1] Department of Astronomy and Astrophysics, Tata Institute of Fundamental Research, 1 Homi Bhabha Road, Colaba, Mumbai 400005, India; yash.bhargava 003@tifr.res.in, yash.bhargava@inaf.it
[2] INAF–Osservatorio Astronomico di Cagliari, via della Scienza, 09047, Selargius (CA), Italy
[3] INAF, Istituto di Astrofisica Spaziale e Fisica Cosmica, Via U. La Malfa 153, I-90146 Palermo, Italy
[4] Department of Physics, McGill University, 3600 rue University, Montréal, QC H3A 2T8, Canada
[5] Trottier Space Institute, McGill University, 3550 rue University, Montréal, QC H3A 2A7, Canada
[6] Indian Institute of Astrophysics, Koramangala II Block, Bangalore 560034, India
[7] Key Laboratory of Particle Astrophysics, Institute of High Energy Physics, Chinese Academy of Sciences, Beijing 100049, People's Republic of China
[8] MIT Kavli Institute for Astrophysics and Space Research, Massachusetts Institute of Technology, Cambridge, MA 02139, USA
[9] Department of Physics, Indian Institute of Technology Hyderabad, IITH main road, Kandi 502284, India
[10] Eureka Scientific, Inc., 2452 Delmer Street, Oakland, CA 94602, USA
[11] Astrophysics, Department of Physics, University of Oxford, Keble Road, Oxford OX1 3RH, UK
[12] INAF—Osservatorio Astronomico di Roma, Via Frascati 33, I-00076, Monte Porzio Catone (RM), Italy
*Received 2024 November 1; revised 2025 May 13; accepted 2025 May 16; published 2026 May 11*

## Abstract

We present the first X-ray polarization measurement of the neutron star low-mass X-ray binary and Z-source, GX 340+0, in the normal branch (NB) using a 200 ks observation with the Imaging X-ray Polarimetric Explorer (IXPE). This observation was performed in 2024 August. Along with IXPE, we also conducted simultaneous observations with NICER, AstroSat, Insight-HXMT, the Australia Telescope Compact Array (ATCA), and the Giant Metrewave Radio Telescope (GMRT) to investigate the broadband spectral and timing properties in the X-ray and radio wavelengths. During the campaign, the source traced a complete Z-track during the IXPE observation but spent most of the time in the NB. We measure X-ray polarization degree (PD) of 1.3% ± 0.3% in the 2–8 keV energy band with a polarization angle (PA) of 38° ± 6°. The PD in the NB is observed to be weaker than in the horizontal branch (HB) but aligned in the same direction. The PD of the source exhibits a marginal increase with energy, while the PA shows no energy dependence. The joint spectro-polarimetric modeling is consistent with the observed X-ray polarization originating from a single spectral component from the blackbody, the Comptonized emission, or reflection feature, while the disk emission does not contribute toward the X-ray polarization. GMRT observations at 1.26 GHz during HB had a tentative detection at 4.5 ± 0.7 mJy, while ATCA observations a day later during the NB detected the source at 0.70 ± 0.05 mJy and 0.59 ± 0.05 mJy in the 5.5 and 9 GHz bands, respectively, suggesting an evolving jet structure depending on the Z-track position.

*Unified Astronomy Thesaurus concepts:* X-ray binary stars (1811); Accretion (14); Stellar accretion disks (1579); Polarimetry (1278); X-ray astronomy (1810)

## 1. Introduction

Z-sources are a unique subclass of accreting neutron star (NS) low-mass X-ray binaries (LMXBs). These sources trace a characteristic Z-shaped track on their X-ray hardness–intensity diagrams (HIDs) or color–color diagrams and, based on their brightness and estimated distances, are expected to accrete close to the Eddington limit (M. van der Klis 2004). These sources host a low magnetic field NS ($10^{8-9}$ G). The spectrum of NS X-ray binary (XRBs) has been historically modeled as either a combination of a multicolor blackbody (e.g., an accretion disk) and a nonthermal component (Eastern model; e.g., K. Mitsuda et al. 1989) or a single temperature blackbody (surface emission from the NS) and a nonthermal component (Western model; e.g., N. E. White et al. 1988). The nonthermal component in either case is often modeled as a Comptonized plasma of hot electrons and could have either a shell-like geometry (where the hot plasma covers the NS and upscatters the photons from the surface; e.g., A. Gnarini et al. 2022) or a slablike geometry (where the plasma is like a sandwich around the accretion disk; e.g., A. Gnarini et al. 2022). The emission could also arise from the boundary layer (BL), due to matter between the accretion disk and the NS (N. I. Shakura & R. A. Sunyaev 1988), or the spreading layer (SL) where matter accreted from the disk partially covers the NS surface (I. I. Lapidus & R. A. Sunyaev 1985; N. A. Inogamov & R. A. Sunyaev 1999).

The characteristic Z-track can be divided into three main branches: the horizontal branch (HB), the normal branch (NB), and the flaring branch (FB), with the hard apex connecting HB and NB and the soft apex connecting NB and FB (G. Hasinger & M. van der Klis 1989). Some Z-sources also show a branch beyond the FB, often called the extended FB (EFB; P. G. Jonker et al. 2000; M. J. Church et al. 2010;

A. Gibiec et al. 2011). In the known set of NS LMXBs, only a few sources persistently show Z-source like behavior: Sco X-1, GX 17+2, GX 349+2, Cyg X-2, GX 5−1, GX 340+0, GX 13 +1 and LMC X-2 (G. Hasinger & M. van der Klis 1989; A. P. Smale et al. 2003; J. K. Fridriksson et al. 2015; M. A. Kaddouh et al. 2024) while some sources (XTE J1701 −462, IGR J17480−2446 and Cir X-1) have intermittently shown a Z-track in their HID indicating that these tracks are strongly related to changes in the accretion rate (J. Homan et al. 2007; D. Lin et al. 2009; J. Homan et al. 2010; M. Chakraborty et al. 2011; J. K. Fridriksson et al. 2015; M. Ng et al. 2024). The shapes of the "Z" on the HID are canonically of two types: Cyg-like, where the track length of the HB and the NB are roughly similar (seen in Cyg X-2, GX 5-1 and GX 340+0; G. Hasinger & M. van der Klis 1989), and Sco-like where the track lengths of the NB and the FB are similar and the HB is significantly shorter (seen in Sco X-1, GX 17+2, GX 349+2, GX 13+1 and LMC X-2; G. Hasinger & M. van der Klis 1989; A. P. Smale et al. 2003; M. A. Kaddouh et al. 2024).

The jets observed from Z-sources show strong variability as the mass accretion rate changes as it traverses along its Z-shaped path in the HID (e.g., W. Priedhorsky et al. 1986; R. M. Hjellming et al. 1990a, 1990b). This variability arises as the structure and properties of the jet change with the changing mass accretion rate, like the state transitions detected in other XRBs (e.g., R. P. Fender et al. 2004b; S. Migliari & R. P. Fender 2006). In the few cases that dedicated, high-cadence radio monitoring has been carried out on Z-sources, the radio emission from the steady jet is generally seen to increase in luminosity as the source moves along the HB toward the NB (e.g., S. Migliari et al. 2007). Around the transition from the HB to the NB, bright, flaring, optically thin radio emission is detected, consistent with the launching of the transient jet. That emission fades throughout the NB, becoming radio faint during the FB. As the source then transitions back through the FB toward the HB via the NB, the source rebrightens in the radio once again (E. B. Fomalont et al. 2001a, 2001b; C. F. Bradshaw et al. 2003; M. Bałucińska-Church et al. 2010; M. J. Church et al. 2012). In addition, it has been proposed that ultra-relativistic ejecta may be launched close to the transition between the NB and the FB, which causes bright radio flares as the ultrarelativistic ejecta collide with the downstream jet (R. Fender et al. 2004a; S. E. Motta & R. P. Fender 2019).

GX 340+0 is a bright Cyg-like Z-source that shows all Z-track branches. It has demonstrated a quick tracing of the complete Z-track, on a timescale of a few days (P. G. Jonker et al. 2000), indicating a rapid change in spectral states. On the other hand, during some of the few day-long observations, the source remained stable in one of the branches (e.g., mainly within the NB with rapid excursions to the FB, or mainly in the HB with no/few excursions to the NB; P. G. Jonker et al. 2000; E. Seifina et al. 2013). GX 340+0 lies in a direction of high line of sight absorption column ($2.2 \times 10^{22}$ cm$^{-2}$; HI4PI Collaboration et al. 2016) and the source also has a high intrinsic absorption column (as indicated by $n_{\rm H} \approx$ (6–12) $\times$ $10^{22}$ cm$^{-2}$ in the literature; M. J. Church et al. 2006; R. Iaria et al. 2006; Y. Bhargava et al. 2023, hereafter B23). The X-ray spectral modeling revealed the presence of multiple emission components, often characterized as a combination of thermal and nonthermal components (M. J. Church et al. 2006; E. Seifina et al. 2013, B23) across all branches. Infrared observations of the source have been able to identify a possible counterpart (B. W. Miller et al. 1993), while radio observations have shown a strong variation of the radio flux as a function of the Z-track position (W. Penninx et al. 1993; T. Oosterbroek et al. 1994; S. G. H. Berendsen et al. 2000). Recent radio observations taken in the HB also indicated a spectral break somewhere between 1.2 and 5.5 GHz, likely a result of synchrotron self-absorption, or free–free absorption, as well as an evolving radio jet (Y. Bhargava et al. 2024, hereafter Paper I).

GX 340+0 was observed with IXPE in 2024 March when the source was mainly within the HB (Paper I; F. La Monaca et al. 2024a). The model-independent polarization in the 2–8 keV energy band was estimated to be 4.0% ± 0.4% with a polarization angle (PA) of 38° ± 3°. The PA of the lowest energy bin (2–2.5 keV) was hinted to be different from the rest of the energy band, indicating a different origin of the polarized emission. The spectro-polarimetric analysis of joint IXPE-AstroSat observation using the spectral model from B23 suggested that the polarized 2–2.5 keV emission could arise from the accretion disk, while the polarized emission above 2.5 keV could be attributed solely to the Comptonized emission or from a contribution of both blackbody and Comptonized emission (Paper I). Alternatively, the spectrum of the source can also be decomposed with the Eastern model, where the accretion disk is expected to account for the low energy (LE) polarization and the corona contributes to the high energy (HE) polarization (F. La Monaca et al. 2024a). The observed polarization degree (PD) of GX 340+0 in the HB matches well with the X-ray polarization seen in the HB from other Z-sources (e.g., XTE J1701−462 and GX 5−1 M. Cocchi et al. 2023; S. Fabiani et al. 2024, respectively). Other, similar, sources that have been observed in the NB and the FB report a lower PD of 0.6%–2% (Cyg X-2, XTE J1701 −462, GX 5−1, Sco X-1 and Cir X-1; M. Cocchi et al. 2023; R. Farinelli et al. 2023; S. Fabiani et al. 2024; F. La Monaca et al. 2024b; J. Rankin et al. 2024, respectively) suggesting a strong geometrical change as the spectral states change.

The IXPE observation of the GX 340+0 reported by Paper I was disrupted due to a spacecraft anomaly, with the rest of the observation occurring from 2024 August 12–16. We supplemented this second IXPE observation with an extensive campaign involving various X-ray and radio facilities. In this article, we report the results from this second campaign and compare them with the insights from the previous campaign conducted in 2024 March. We describe the data reduction procedures for individual instruments in Section 2, detail the analysis methodologies and results in Section 3, and interpret the results in Section 4.

## 2. Observations and Data Reduction

### 2.1. IXPE

IXPE conducted a ≈200 ks observation of GX 340+0 from 2024 August 12 to 16. The details of the observations are listed in Table 1. We used `ixpeobssim` software (v31.0.1) to bin the event data (F. Kislat et al. 2015; L. Baldini et al. 2022) into the high-level products (e.g., energy-dependent light curves, Stokes I, Q, and U spectra, and model-independent polarization properties with the PCUBE algorithm). The event data were calibrated and weighted according to the calibration files corresponding to the recent calibration epoch of 2024 July 1

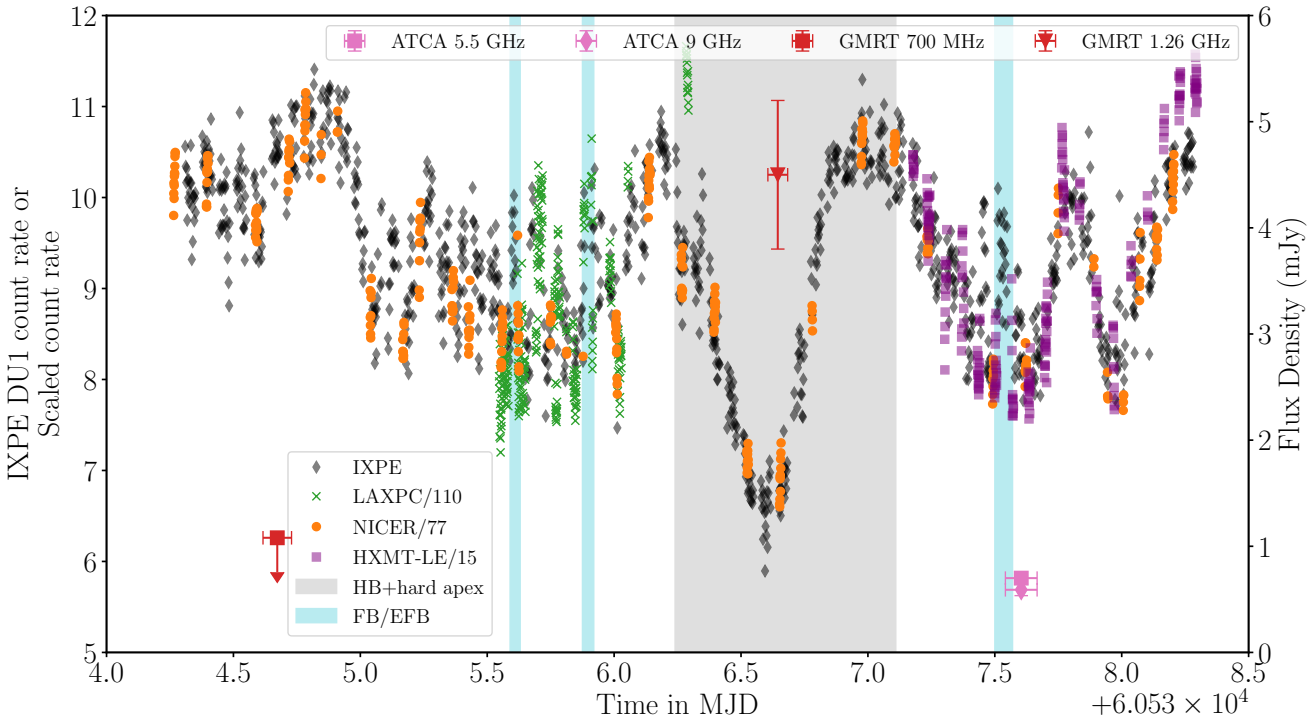


**Figure 1.** The evolution of GX 340+0 as seen by IXPE is shown as black diamonds. The IXPE observation was supplemented with joint observations with NICER (in orange circles), AstroSat (LAXPC light curve as green crosses), and Insight-HXMT (LE light curve as purple squares). The observation log of these instruments is noted in Table 1. The light curves from NICER, AstroSat-LAXPC, and Insight-HXMT/LE are scaled to highlight the similarity in the joint observations, and the scaling factors are mentioned in the legend of the plot. Additionally, we also show results from radio observations conducted during the X-ray campaign, shown as the magenta and red points (where the radio flux density can be read on the right *y*-axis). The intervals for the FB/EFB and the HB (including the hard apex) are indicated by the cyan and gray shaded regions, respectively. The source was in the NB at all other times (see Table 2 for exact time stamps of NB intervals).

**Table 1**
Observation Log for the Multiwavelength Campaign of GX 340+0

| Observatory | Instrument | Observation ID | Start Time | Stop Time |
|---|---|---|---|---|
| IXPE | Gas Pixel Detector (DU1–3) | 03009901 | 2024-08-12 07:26:35 | 2024-08-16 06:45:03 |
| NICER | X-ray Timing Instrument | 7705010101 | 2024-08-12 06:20:47 | 2024-08-12 21:51:37 |
| | | 7705010102 | 2024-08-13 00:55:35 | 2024-08-13 21:03:55 |
| | | 7705010103 | 2024-08-14 00:08:50 | 2024-08-14 23:31:20 |
| | | 7705010104 | 2024-08-15 02:27:38 | 2024-08-15 22:41:48 |
| | | 7705010105 | 2024-08-16 00:08:37 | 2024-08-16 04:56:07 |
| AstroSat | LAXPC | 9000006386 | 2024-08-13 13:07:31 | 2024-08-14 07:01:41 |
| *Insight*-HXMT | LE | P061437700402- | 2024-08-15 04:14:58 | 2024-08-16 07:07:50 |
| | ME | P061437700410 | 2024-08-15 04:14:28 | 2024-08-16 07:57:19 |
| GMRT | Band 4 | ddtC367 | 2024-08-12 14:47:47 | 2024-08-12 17:29:42 |
| GMRT | Band 5 | ddtC367 | 2024-08-14 14:32:23 | 2024-08-14 16:24:42 |
| ATCA | ··· | | 2024-08-15 13:43:40 | 2024-08-15 15:49:40 |

(`obssim20240701_alpha075`; A. Di Marco et al. 2022) for the light curves and spectra, and the unweighted calibration files were used for PCUBE (`obssim20240701`; A. Di Marco et al. 2022; S. V. Forsblom et al. 2024). For the extraction of the source photons, we adopted a 1.′6 circular region. Since the count rate of the source was higher than 2 c $s^{-1}$ $arcmin^{-2}$ (see Figure 1), we do not perform any background rejection or subtraction (as suggested in A. Di Marco et al. 2023). For the model-independent analysis, the polarization information from individual detection units (DUs) was combined and reported in Section 3.3.1. For the spectral analysis, we rebinned the I spectrum to ensure at least 25 counts per bin (to enable $\chi^2$ statistics). The Stokes Q/U spectra were not rebinned as they had a similar number of bins as the Stokes I spectra in the operational energy range of 2–8 keV.

### 2.2. *Neutron Star Interior Composition Explorer*

The Neutron star Interior Composition Explorer (NICER; K. C. Gendreau et al. 2016) is a nonimaging instrument onboard the International Space Station, comprising 56 silicon drift detectors and X-ray concentrator optic pairs (52 operational) in focal plane modules (FPM). NICER observed GX 340+0 between 2024 August 12 and 2024 August 16 (see

**Table 2**
Start and End Times of Identified NB Intervals

| Start MJD | End MJD |
|---|---|
| 60534.30 | 60535.59 |
| 60535.63 | 60535.69 |
| 60535.72 | 60535.87 |
| 60535.92 | 60536.24 |
| 60537.11 | 60537.50 |
| 60537.57 | 60538.40 |

**Note.** The intervals mentioned here include the data gaps evident in the light curves (see Figure 1).

Table 1), within the IXPE observation interval. The raw data were reduced and processed using `HEASOFT` version 6.33 and the NICER Data Analysis Software (`NICERDAS`) version 12 (2024-02-09_V012) using calibration version `xti20240206`. We employed the following filtering criteria in generating the good time intervals: NICER being outside of the South Atlantic Anomaly; angular offset for the source of $<54''$; Earth limb elevation angle $>20°$; undershoot rate of 0–500 $c^{-1}s^{-1}FPM^{-1}$; overshoot rate of 0–30 $c^{-1}s^{-1}FPM^{-1}$, and a minimum cutoff rigidity such that `COR_SAX>` 1.5. The processing was done using the `threshfilter=DAY` as the observations were taken during the orbital day, and thus, the lowest energy data may be affected. To investigate the branch-resolved behavior of the source, we first combined the observations using `niobsmerge`. These filtering criteria resulted in a total exposure of 15.3 ks for scientific analysis. We generated spectral products (including response matrices) using `nicerl3-spect`, where we grouped the spectra with the optimal binning scheme (J. S. Kaastra & J. A. M. Bleeker 2016) and rebinned the spectra such that each bin had a minimum of 25 counts. We also generated light curves in various energy bands (the 0.5–10 keV light curve binned at 50 s is shown in Figure 1 in orange circles) using `nicerl3-lc`. Using the time intervals for which we identified the source to be in the different branches (see Section 3.1 for details on the state identification and Table 2 for the NB intervals), we constructed the spectrum from the merged event file for the NB intervals and extracted the appropriate response and auxiliary response files. For estimating the background, we made use of the SCORPEON model (C. Markwardt et al. 2024).

### 2.3. AstroSat

To supplement the IXPE observation with broad X-ray energy coverage, we conducted a target-of-opportunity observation with AstroSat (K. P. Singh et al. 2014), running 2024 August 13–14. For the observation, we used the Large Area X-ray Proportional Counter (LAXPC; J. S. Yadav et al. 2016, 2017) as the primary instrument. We procured the level 1 data of the LAXPC observation from AstroBrowse[13] and reduced the data using relevant tools in LAXPCSOFTWARE22AUG15.[14] (H. M. Antia et al. 2021; R. Misra et al. 2021). The pipeline also includes the tools to filter the South Atlantic Anomaly passage and Earth occultation intervals and extract the energy-dependent light curves, spectra, background spectra, and background light curves. For the analysis, we considered only LAXPC 20, as LAXPC 30 was turned off early in the mission, and LAXPC 10 indicated abnormal gain variation. To minimize the background contribution over 3–20 keV, we used the layer 1 data for the extraction of higher-level products (e.g., light curves and spectra). We show the scaled light curve (binned at 50 s) from the LAXPC observation in Figure 1 as green crosses. The spectrum from LAXPC was rebinned according to the detector response. Due to response uncertainties, we included a 2% systematic error in the spectrum across the complete energy range (3–20 keV).

### 2.4. Insight-HXMT

Insight-HXMT (S.-N. Zhang et al. 2020) observed GX 340 +0 from 2024 August 15, 00:44:17 to 2024 August 16, 08:28:41. The data were extracted from all three instruments using the Insight-HXMT Data Analysis software v2.06,[15] and filtered with the following standard criteria: (1) pointing offset angle less than $0.^{\circ}04$; (2) Earth elevation angle larger than 10°; (3) the value of the geomagnetic cutoff rigidity larger than 8 GV; (4) at least 300 s before and after the South Atlantic Anomaly passage. To avoid possible contamination from the bright Earth and nearby sources, we only use data from the small field of view detectors (Y. P. Chen et al. 2018). The software also provides the relevant response and background files for the spectral analysis. The HE data are not used in our spectral analysis as the HE spectra were dominated by the background. The energy bands adopted for spectral analysis are 2–10 keV for LE and 10–20 keV for medium energy (ME). The scaled light curves from Insight-HXMT-LE in 3–10 keV and binned at 50 s are shown in Figure 1 as purple circles.

### 2.5. Giant Metrewave Radio Telescope

We observed GX 340+0 with the Giant Metrewave Radio Telescope (GMRT). Utilizing the wideband receiver backend of GMRT, data were recorded in two frequency bands: band 4 (central frequency 750 MHz, bandwidth 400 MHz) and band 5 (central frequency 1260 MHz, bandwidth 400 MHz) on 2024 August 12 and 2024 August 14, respectively (Proposal ddtC367, for simultaneous coverage with the IXPE campaign). The raw data were downloaded in the `FITS` format and converted to the Common Astronomy Software Applications (`CASA`; CASA Team et al. 2022) measurement set format. The data were calibrated (3C286 was used for flux and bandpass calibration, and J1717-398 was used for phase calibration) and imaged using the automated continuum imaging pipeline `CASA-CAPTURE` (R. Kale & C. H. Ishwara-Chandra 2021). Manual flagging and calibration were performed as required. Eight rounds of self-calibration (both phase and amplitudes) were completed within each pipeline run to obtain the final cleaned images. No sources were detected at the position of GX 340+0 in the band 4 observations, providing a $3\sigma$ upper limit of 1.1 mJy at 750 MHz, where we use the rms of the noise from a large area in a source-less region of the image (close to the source position) as $\sigma$. The band 5 data were heavily affected by radio frequency interference, but the image shows a tentative point source close to the known position of GX 340+0 with a flux density, $S_{\nu}$, of 4.5 ± 0.7 mJy at 1.26 GHz (10% flux density error added in quadrature to the

[13] https://astrobrowse.issdc.gov.in/astro_archive/archive/Home.jsp
[14] http://astrosat-ssc.iucaa.in/uploads/laxpc/LAXPCsoftware22Aug15.zip
[15] The data analysis software is available from http://hxmten.ihep.ac.cn/software.jhtml.

rms in a large source-less region to obtain the error in the maximum).

### 2.6. Australia Telescope Compact Array

The Australia Telescope Compact Array (ATCA) observed GX 340+0 on 2024 August 15 between 13:43:40 and 15:49:40 UT. During the observation, ATCA was in a relatively extended 1.5 km configuration.[16] Data were recorded simultaneously at central frequencies of 5.5 and 9 GHz, with 2 GHz of bandwidth at each frequency band. We used PKS B1934−638 for flux and bandpass calibration, and the nearby calibrator J1631−4345 for phase calibration. Data were flagged, calibrated, and imaged using standard procedures within the (CASA version 5.3.1; CASA Team et al. 2022). Imaging used a Briggs robust parameter of 0, balancing sensitivity and resolution. Fitting for a point source in the image plane, GX 340+0 was detected at both central frequencies, where $S_\nu = 0.70 \pm 0.05$ mJy at 5.5 GHz and $0.59 \pm 0.05$ mJy at 9 GHz. This corresponds to a radio spectral index, $\alpha$, of $-0.35 \pm 0.25$ (defined as $S_\nu \propto \nu^\alpha$, where $\nu$ is the frequency). Such a radio spectral index could be consistent with a steep spectrum from transient ejecta, or a flat radio spectrum from a steady jet.

To explore intraobservational variability, we also imaged the source on 20 minute timescales. We found that at both central frequencies the flux density decreased for the first ∼half of the observation, before remaining stable during the second half. At 5.5 GHz, the flux density decreased from $1.07 \pm 0.15$ mJy at the start of the observation to $0.44 \pm 0.10$ mJy by the middle of the observation. During the second half of the observation, the 5.5 GHz flux density then remained stable (within errors), measuring $0.50 \pm 0.10$ mJy at the end of the observation. At 9 GHz, the flux density was measured to be $0.82 \pm 0.08$ mJy at the start, dropping to $0.32 \pm 0.06$ mJy by the middle of the observation, remaining stable (within errors) to the end of the observation, $0.34 \pm 0.10$ mJy.

## 3. Data Analysis and Results

### 3.1. Identification of the States

Previous IXPE observations of Z-sources have indicated that the X-ray polarization from these systems is dependent on the branch position. Thus, we need to identify the source state throughout the observation to interpret the nature of X-ray polarization and, therefore, the emission components. We constructed the HID using all the X-ray instruments using different definitions of hardness (typically limited by the energy range from the instruments) and have shown them in Figure 2.

From the HID, GX 340+0 traced the complete Z-track during the observation. The HID from NICER (count rate in 3–10 keV and hardness ratio (HR) as the ratio between 5–10 and 3–5 keV bands) can identify the epochs when the source was in the HB and the NB while the HID from AstroSat-LAXPC (count rate in 3–20 keV and HR as the ratio between 10–20 and 6–10 keV bands) highlights the track from the hard apex to the EFB. The Insight-HXMT observation (HID constructed using the LE and ME light curves in the 6–10 and 10–20 keV bands, respectively) was mainly in the NB, but for some duration the source seemed to indicate an excursion in the FB (as seen below the HR of 0.8 in the bottom right panel of Figure 2). The identified FB/EFB and HB intervals are marked in the IXPE HID. Notably, the FB/EFB intervals are not distinguishable from NB solely based on the HID (see the Appendix for a deeper investigation).

For this study, we identified FB intervals using the AstroSat-LAXPC and Insight-HXMT HID and extrapolated the intervals to the data gaps (if present) using the fact that Z-sources continuously move along the Z-track without jumping between branches (e.g., M. J. Church et al. 2006; J. Homan et al. 2007; K. Sriram et al. 2011; D. Lin et al. 2012, B23). Since we focus on the analysis of the NB, these intervals are excluded from any estimation of the polarization or the spectrum. A possible caveat in the state identification is that during the intervals where the source was covered by only NICER and IXPE, there may be some FB/EFB intervals that have been misclassified as NB. The similarity of the FB/EFB and NB in the HID in the soft X-ray emission (e.g., Figure 5) would suggest a similarity in the spectrum of these two branches (at least $\lesssim$10 keV). Since the states seem to be indistinguishable in the HID, we assume that the inclusion of these segments during the NB does not affect the spectral or polarimetric results significantly.

### 3.2. Spectral Modeling of NB

To understand various spectral components from the GX 340+0 during the NB, we extracted the spectra for all instruments using the methods described in their respective sections (Sections 2.1–2.4) for the intervals corresponding to the NB (Table 2). During the epochs of the AstroSat and Insight-HXMT observations, we excluded any FB/EFB intervals as determined in Section 3.1. We conducted the spectral and spectro-polarimetric modeling in XSPEC V12.14.1. For fitting the spectra, we used PGstat for NICER spectra (as the background estimation for NICER observations is done by SCORPEON modeling and results in a non-Poissonian background) and $\chi^2$ for the rest of the spectra. We used $\chi^2$ as the test statistic and report $1\sigma$ confidence intervals for the estimated parameters.

Since the focus of the analysis is to identify the spectral components responsible for the X-ray polarization, we utilized the joint coverage of IXPE and NICER to identify the spectral components. We also included the spectrum from AstroSat-LAXPC as it overlapped with NICER and IXPE, and allows us to extend the spectral range to 20 keV, placing a strong constraint on the hard X-ray emission, primarily the non-thermal component. At the softest energies (<0.6 keV), the NICER spectrum was dominated by the noise peak due to additional optical loading from the orbital day. Thus, we ignored the NICER spectrum below 0.6 keV. In case of spectra from other instruments, we excluded the energy intervals where the background counts were higher than the source counts. We note that the inclusion of Insight-HXMT spectra in the joint fit resulted in a bad fit for all instruments. A better fit was obtained if we allowed one set of parameters for IXPE, NICER, and AstroSat-LAXPC and one set of parameters for Insight-HXMT, which could be due to calibration mismatch between these instruments. Since the inclusion of Insight-HXMT spectra did not provide any additional information over joint IXPE, NICER, and AstroSat-LAXPC spectra, we report the analysis of the latter set of spectra. The individual

[16] https://www.narrabri.atnf.csiro.au/operations/array_configurations/configurations.html

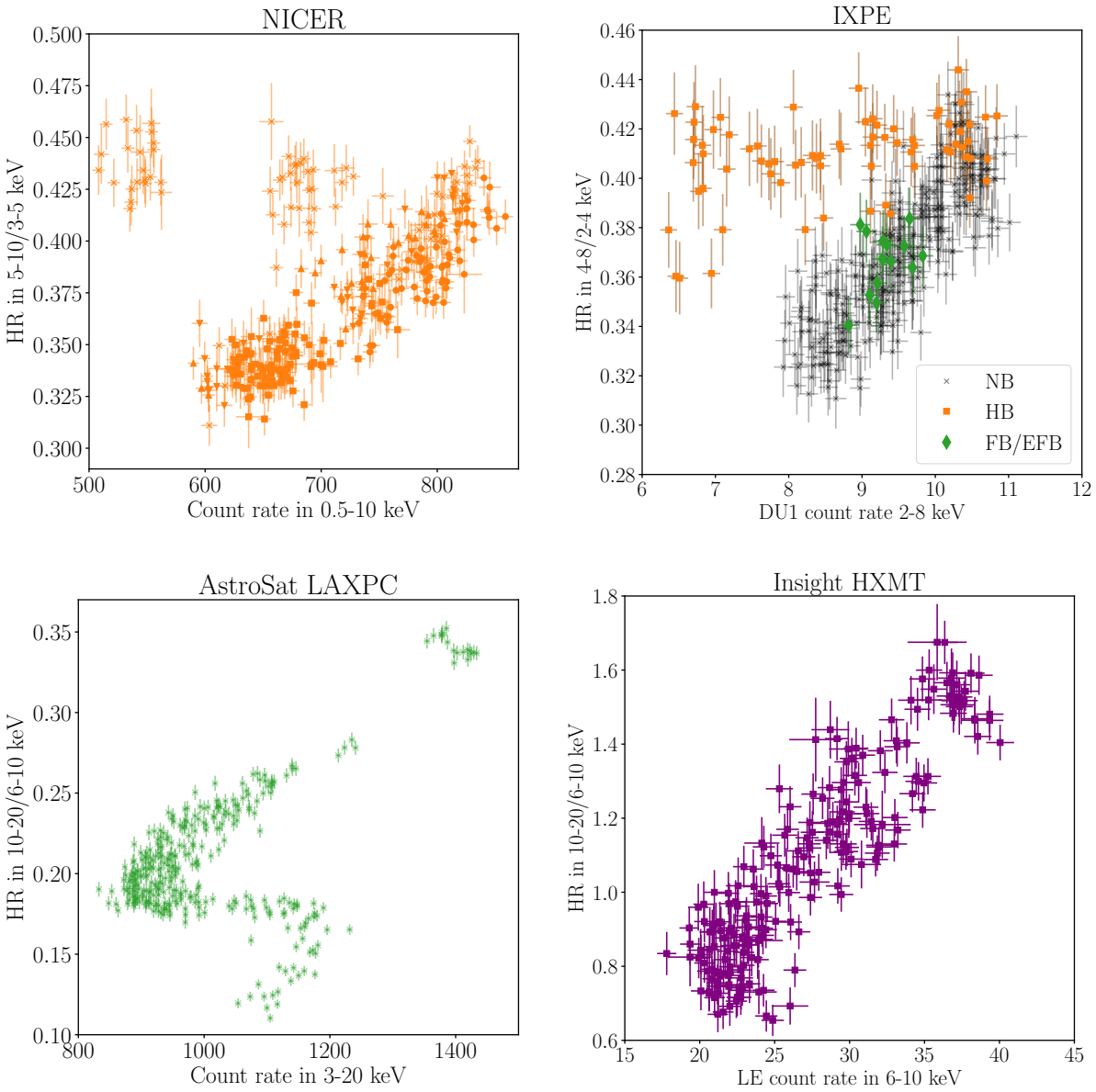


**Figure 2.** HIDs of GX 340+0 as seen by different observatories during the X-ray and radio campaign. The NICER and AstroSat HIDs (top left and bottom left, respectively) indicate that the source traversed through all the states during the campaign. Comparing the HID and light curve in Figure 1, we can infer that the source went into the HB only once (during the big dip from MJD 60536.24-60537.11). During the rest of the time, the source was in the NB with a few excursions into the FB and EFB. The HID from the IXPE observation (top right) is able to distinguish the HB (shown as the orange squares) from the NB (black crosses) around the apex. In addition, the IXPE points that lie within the FB/EFB intervals, as identified from AstroSat and Insight-HXMT, are shown with green diamonds and are clearly not identifiable solely from the IXPE HID. The Insight-HXMT HID is generated by taking a ratio of ME in 10–20 keV and LE in 6–10 keV to see if the source underwent a transition to FB. The HID seems to indicate a slight bend into FB.

IXPE-DU spectra suggested differences in the calibration, and therefore, we left the gain slope and offset parameter free during the initial modeling (e.g., F. La Monaca et al. 2024a) and fixed them to best-fit values for the computation of the confidence intervals on the spectral parameters. The typical gain offset for each spectrum was found to be $\lesssim$5% (see Table 3 for the estimated gain parameters).

Noting a high absorption column modeled in the literature of the source (e.g., M. J. Church et al. 2006; R. Iaria et al. 2006), we modeled the absorption column with `tbabs` and used the abundances from J. Wilms et al. (2000) and cross sections from D. A. Verner et al. (1996). Initially, we modeled spectra from individual observatories to identify the minimum number of additive components required to sufficiently model them. We fit the spectra with `tbabs*nthcomp`, which assumes that the nonthermal component arises from a Comptonizing medium (A. A. Zdziarski et al. 1996; P. T. Życki et al. 1999), which is upscattering photons from an accretion disk. We observed that this combination resulted in an unacceptable fit statistic ($\chi^2$/degrees of freedom or d.o.f. = 4233/601). The residuals clearly indicated the presence of a softer component, which we modeled with a blackbody (`bbodyrad`). The inclusion of a blackbody component resulted in a lower test statistic ($\chi^2$/d.o.f. = 2531/599), but the fit was still not acceptable. The NICER and IXPE spectra indicated the presence of iron line emission that was modeled with a `Gaussian`. For the AstroSat-LAXPC data, the normalization of the `Gaussian` component was observed to be lower than that of other instruments (which could be due to calibration mismatch). The resulting $\chi^2$ of 1877 for 595 d.o.f. was still not

**Table 3**
Spectral Modeling of GX 340+0 during the NB

| Component | Parameter | Unit | Value |
|---|---|---|---|
| tbabs | $n_H$ | $10^{22}$ cm$^{-2}$ | $9.62^{+0.09}_{-0.14}$ |
| diskbb | $kT_{disk}$ | keV | $0.212^{+0.003}_{-0.006}$ |
| | Norm[a] | $10^5$ | $9.9^{+1.6}_{-1.5}$ |
| bbodyrad | $kT_{bb}$ | keV | $0.983^{+0.008}_{-0.008}$ |
| | Norm[b] | ... | $782^{+18}_{-25}$ |
| nthcomp | $\Gamma$ | ... | $2.25^{+0.02}_{-0.03}$ |
| | $kT_e$ | keV | $3^{+1}_{-1}$ |
| | $kT_{seed}$ | keV | $= kT_{disk}$ |
| | Norm[c] | ... | $3.2^{+0.1}_{-0.2}$ |
| Gaussian | LineE | keV | $6.25^{+0.06}_{-0.12}$ |
| | LineW | keV | $2.0^{+0.07}_{-0.04}$ |
| | LineN[d] | ... | $0.19^{+0.02}_{-0.01}$[e] |
| edge | EdgeE | keV | $1.823^{+0.005}_{-0.002}$ |
| | $\tau$ | ... | $0.190^{+0.011}_{-0.007}$ |
| constant | $C_{DU1}$ | ... | 0.648 |
| | $C_{DU2}$ | ... | 0.655 |
| | $C_{DU3}$ | ... | 0.646 |
| | $C_{LAXPC}$ | ... | 0.879 |
| Gain Parameters | | | |
| Instrument | Parameter | Unit | Value |
| IXPE-DU1 | Slope | ... | 0.998 |
| | Offset | eV | 2 |
| IXPE-DU2 | Slope | ... | 0.990 |
| | Offset | eV | 44 |
| IXPE-DU3 | Slope | ... | 0.996 |
| | Offset | eV | 24 |
| Fitting Statistic | | | |
| Instrument | Statistic | | Value (Stat/Bins) |
| NICER | PG | | 275.8/146 |
| IXPE-DU1 | $\chi^2$ | | 210.5/148 |
| IXPE-DU2 | $\chi^2$ | | 183.6/148 |
| IXPE-DU3 | $\chi^2$ | | 176.2/148 |
| LAXPC | $\chi^2$ | | 6.34/20 |
| Test Statistic: $\chi^2$/ d.o.f. | | | 670.7/592 |

**Notes.** The model decomposition used for the following table is constant*tbabs*(diskbb+bbodyrad+nthcomp+Gaussian)*edge.
[a] The disk normalization is defined as Norm $=(R_{\rm eff}/D_{10})^2*\cos\theta$, where $R_{\rm eff}$ is the apparent inner radius of the accretion disk in km, $D_{10}$ is the distance to the source in units of 10 kpc, and $\theta$ is the inclination angle of the disk.
[b] The blackbody normalization is defined as $=(R/D_{10})^2$, where $R$ is the radius of the emission region in km.
[c] The normalization of nthcomp is defined as counts s$^{-1}$ cm$^{-2}$ keV$^{-1}$ at 1 keV.
[d] The normalization of the Gaussian component is the photons cm$^{-2}$ s$^{-1}$ in the line.
[e] For LAXPC, the Gaussian normalization was estimated at $4^{+8}_{-2}\times 10^{-3}$ photons cm$^{-2}$ s$^{-1}$.

acceptable, where the residuals indicated the presence of a softer component and possibly an edge at 1.8 keV. We described this component as an accretion disk modeled with a soft multicolor blackbody (i.e., diskbb) and tied the inner disk temperature to the seed photon temperature for the nthcomp component ($\chi^2$/d.o.f. = 698.6/594). After the inclusion of diskbb, the residuals at the highest energies were accounted for, as now the Comptonized emission could describe the emission at higher energies without the need to compensate at softer energies.[17] We note that the reduced $\chi^2$ is not acceptable at this stage, and the fitting statistic of the NICER spectra could be further reduced by modeling the edge-like residuals with a multiplicative component edge. After the inclusion of the edge component, the test statistic of $\chi^2$/d.o.f. = 670.7/592 is acceptable (as compared to the previous case of the model without the edge, using either the Akaike information criterion or Bayesian information criterion). The spectral parameters are noted in Table 3. To compute the confidence intervals for various spectral parameters, we sampled the parameter space using a Markov Chain Monte Carlo sampler in XSPEC. We used the Goodman–Weare algorithm and initialized 30 walkers close to the best-fit parameters and ran for a total of 9000 steps after a 1980 burn-in steps. The confidence intervals were determined from the marginalized distribution of the sampled parameter space. We also show the count spectra from various instruments, the unfolded model, and residuals from all the spectra at various stages of spectral modeling in Figure 3.

### 3.3. Polarization in NB

Using the NB intervals as defined in Section 3.1, we investigated the polarization properties in a model-independent manner (see Section 3.3.1), and using the spectral decomposition from Section 3.2 we investigated the spectro-polarimetric properties of GX 340+0 in Section 3.3.2.

#### 3.3.1. Model-independent Analysis

To extract the model-independent polarization properties of GX 340+0 in NB, we used the PCUBE algorithm to bin the IXPE observation. Since the source was well above the background, we did not need to apply any background subtraction or rejection of events (A. Di Marco et al. 2022). We extracted the polarization information for individual detectors and then combined them to enhance the measurement statistics. We measured a PD of 1.3% ± 0.3% and a PA of 38° ± 6° in the 2–8 keV band for the NB intervals. Since we have a highly significant detection, we divided the IXPE operational band into three logarithmically spaced energy bins to extract the model-independent polarization properties. The full band and energy-dependent polarization properties are reported in Table 4 and depicted in Figure 4. The polarization was not significant ($<3\sigma$) in the softest energy band (2.0–3.2 keV), while it is $>3\sigma$ in the 3.2–5.0 keV and 5.0–8.0 keV bands. We also estimated the polarization from the HB and FB/EFB intervals individually (gray and cyan intervals in Figure 1, respectively) and found that the significance of the measurement was $<3\sigma$. Therefore, we placed upper limits on the X-ray polarization during these segments of the IXPE observation for the full 2–8 keV band

[17] We note that the current spectral model is similar to the Western model with the addition of a soft and truncated accretion disk to explain the excess in the softer energies ($\lesssim$2 keV). This particular combination of models has also been tested in previous spectral investigations of GX 340+0 by B23, where a comparison to the Eastern model counterpart (i.e., softest thermal component is a blackbody while component >1 keV is the accretion disk) is discussed extensively.

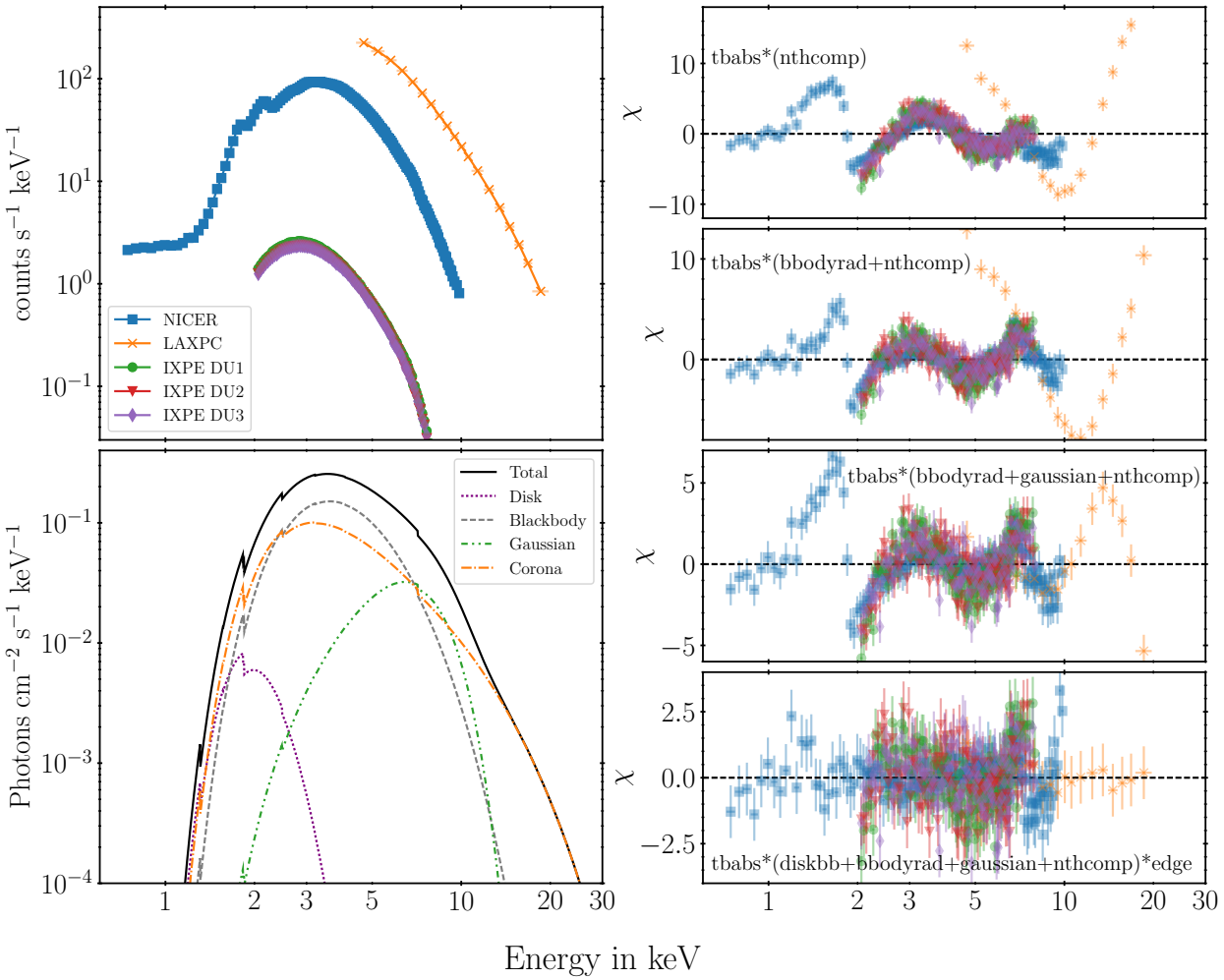


**Figure 3.** Top left: count spectra of GX 340+0 as observed during the NB by various instruments (depicted in different colors and markers indicated in the legend). Bottom left: The best-fit model (`tbabs*(diskbb+bbodyrad+nthcomp+Gaussian)*edge`) used to fit the count spectra is shown in the black solid curve; individual components are shown as various lines (indicated in the legend). Right panels: Residuals ($\chi = \frac{\text{data} - \text{model}}{\text{error}}$) are shown for various intermediate models (noted in individual panels and described in Section 3.2), and the residuals for the best-fit model are shown in the bottommost-right panel.

**Table 4**
Polarization of GX 340+0 during the NB

| Model-independent Polarization | | |
|---|---|---|
| Energy band (keV) | PD (%) | PA (deg) |
| 2.0–8.0 | 1.3 ± 0.3 | 38 ± 6 |
| 2.0–3.2 | 0.9 ± 0.4 | 32 ± 14 |
| 3.2–5.0 | 0.9 ± 0.3 | 32 ± 9 |
| 5.0–8.0 | 1.9 ± 0.5 | 43 ± 9 |

**Note.** $1\sigma$ confidence intervals are reported.

using PCUBE. We found at $3\sigma$ confidence, the HB PD is $<1.8\%$ for a livetime of 42.46 ks, and the FB PD is $<4.3\%$ for a livetime of 8.39 ks.

### 3.3.2. Spectro-polarimetric Modeling

As shown in Figure 3, the 2–8 keV emission has contributions from the blackbody, the corona, and the Gaussian emission components. To investigate the spectro-polarimetric properties of GX 340+0 during the NB, we used the joint spectral fit from Section 3.2 and included the Stokes Q and U spectra from IXPE to model the polarimetric properties. We report $1\sigma$ confidence intervals for the estimated polarization parameters. For this exercise, we fixed the spectral parameters (including the cross-normalization constants) and only allowed polarimetric parameters to be free. To test if the complete emission can be characterized by a single polarization component, we applied `polconst` and `pollin` to all additive components (the model description for constant polarization: `constant*tbabs*polconst*(diskbb+bbodyrad+nthcomp+Gaussian)*edge`, and for linearly dependent polarization, `polconst` was replaced with `pollin`). In case of `polconst`, we note that the $\chi^2$ was 1563.8 for 1502 d.o.f. and the PD is $1.1\% \pm 0.2\%$ for a PA of $33° \pm 5°$. Since the polarization from the polarization cube does not indicate an energy dependence for the polarization angle, we kept the slope of the polarization angle fixed at zero for the POLLIN model. The $\chi^2$ for linear dependence of polarization on energy was 1560.5 for 1501 d.o.f., and the slope of the PD is $0.33^{+0.08}_{-0.18}$, which is consistent with zero within $2\sigma$, indicating that while there may be a marginal dependence of the PD on the energy, our data are not entirely conclusive.

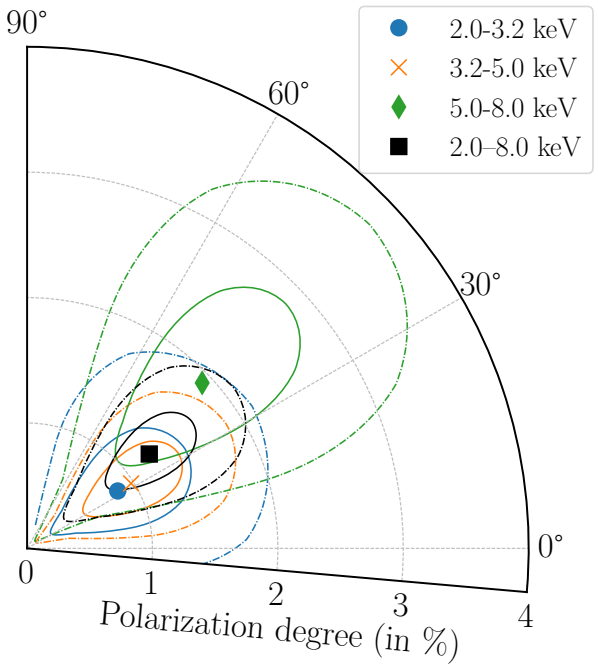


**Figure 4.** Model-independent polarization of GX 340+0 during the NB. The markers depict the estimated PD and PA in the corresponding energy bins, while the solid and dashed lines correspond to $1\sigma$ and $3\sigma$ confidence intervals. Polarization was detected at $>3\sigma$ level in the 3.2–5 keV and 5–8 keV energy bands, and at $>4\sigma$ level for 2–8 keV, but not detected in the 2–3.2 keV energy band.

The energy dependence of X-ray polarization as measured using PCUBE suggests that the softer energy bands have a marginal detection of polarization. To test if the observed model-independent polarization can be explained by a polarization from individual components, we applied `polconst` to `nthcomp`, `diskbb`, and `bbodyrad`. Due to the marginal nature of soft X-ray polarization, we found that the fit is insensitive to any PD value of the disk component; therefore, we keep it fixed to 1%, which is the expected PD from an accretion disk (e.g., L.-X. Li et al. 2009) at an inclination angle of 35° (J. M. Miller et al. 2016). Additionally, we note that we obtain an acceptable fit if the PD of the blackbody component is fixed to zero and the PD and PA of the Comptonized emission are left free ($\chi^2$/dof = 1565.9/1502). In this case, we measured the PD of the Comptonized emission to be 2.76% ± 0.5%, with a PA of 33° ± 5°. An alternative test could be that the polarized emission could instead arise from the BL/SL (i.e., the component modeled with a blackbody). We obtained an equally acceptable fit ($\chi^2$=1566.0) in this case with a PD=1.9% ± 0.4% and PA=32° ± 5°.

## 4. Discussion

X-ray and radio observatories of GX340+0, taken on 2024 August 12–16, show that the source traced its complete Z-track, demonstrating rapid spectral state transitions (P. G. Jonker et al. 2000; J. K. Fridriksson et al. 2015). GX 340+0 traversed from the FB to the HB in less than a day (from MJD 60535.9, where it was in the FB, to MJD 60536.2, where it entered the HB and stayed for about a day, see Figure 1). However, for the majority of our observations, the source resided in the NB.

### 4.1. Polarization in GX 340+0

GX 340+0 has been observed over two epochs with IXPE: once in 2024 March, where it was observed to be in the HB (Paper I; F. La Monaca et al. 2024a), and again in 2024 August, where it showed a complete tracing of the Z-track, but spent the majority of the time in the NB. In this work, we have investigated the polarimetric properties of the source in the NB using the 2024 August observation (see Paper I for a detailed discussion of the 2024 March observations). The observed 2–8 keV PD during the NB (1.3% ± 0.3%, see Table 4) is lower than the PD measured during the HB (4%; Paper I), but the PAs are consistent across both branches. The similarity in the PA indicates that the emission component in the hard X-rays is likely similar across both branches. Assuming the polarization is from a single component, i.e., a Comptonizing medium in both cases, would suggest that the emission has depolarized as the source moves from HB (9%; Paper I) to NB (2.4%; Table 4). A similar decrease in net polarization was observed in simulations by A. Gnarini et al. (2022), where the hard state polarization (similar to the HB in Z-sources) was observed to be higher than the soft state polarization (similar to the NB/FB/EFB in Z-sources). We also estimated the polarization properties for the HB and the FB/EFB segments in the present observation, but the duration was not sufficient to detect polarization significantly, with a minimum detectable polarization at 99% confidence (MDP99) of 1.7% for HB and 3.8% for FB/EFB, respectively. The MDP99 of the HB was lower than the reported value in Paper I and F. La Monaca et al. (2024a), but we only obtained an upper limit of 1.8% at a $3\sigma$ confidence interval. This could be due to either the inclusion of the hard apex in the current analysis or that the source spent insufficient time in the deepest part of the HB for the polarization to be detected significantly (which happened in the 2024 March IXPE observation). The source was observed in FB/EFB for a short duration (8.39 ks), which is not sufficient for a significant detection of polarization (as indicated by a large MDP99). Our observations place a $3\sigma$ upper limit of 4.3% on the PD during these states. The FB/EFB observations of Cyg-like Z-sources are limited to the observation analyzed in this work, while Sco X-1 shows a PD of 1.0% ± 0.2% in its soft apex+FB (F. La Monaca et al. 2024b).

In the softer energies, the X-ray polarization was not significantly detected. Therefore, the slight discrepancy in the PA between 2–2.5 keV and 2.5–8 keV reported by Paper I and F. La Monaca et al. (2024a) during the HB was not constrained in the NB. According to Paper I, the accretion disk emission in 2–2.5 keV was the primary contributor toward the PA difference. In the spectral modeling of the NB data (Section 3.2), we note that the disk appeared more truncated than during the HB (e.g., B23) with a lower contribution in the 2–8 keV band (the flux from `diskbb` component in computed using the parameters in B23 is 5 times higher than disk flux using parameters from Table 3) Therefore, a nondetection of the PA discrepancy is consistent with the spectro-polarimetric decomposition suggested by Paper I.

The X-ray polarization during the NB in GX 340+0 is similar to the other Z-sources, e.g., Cyg X-2: 1.85% ± 0.87% (R. Farinelli et al. 2023), XTE J1701−462: <1.5% (at 99% confidence; M. Cocchi et al. 2023), GX 5−1: 2.0% ± 0.3% (S. Fabiani et al. 2024), and Sco X-1: 1.0% ± 0.2% (F. La Monaca et al. 2024b). Out of these sources, only

XTE J1701−462 and GX 5−1 have been observed in the HB as well (which also match the GX 340+0 HB polarization; M. Cocchi et al. 2023; S. Fabiani et al. 2024; Paper I). The similarity of polarization levels in these sources over different states, along with a similarity in timing signatures (e.g., G. Hasinger & M. van der Klis 1989), hints at a similarity in the geometry of emission components.

The simulations of weakly magnetized NS LMXBs (A. Gnarini et al. 2022) suggest that typical polarization values in HB and NB (which would correspond to hard and soft states in A. Gnarini et al. 2022) match with a slablike corona. However, the simulations also suggest that the PA variation is drastically different for both states. The difference in the PA is due to the assumption that the disk is polarized, and has a significant contribution in the 2–8 keV. If the thermal component is unpolarized (e.g., a blackbody component from the surface), then the PA dependence on energy will be caused by a single component (i.e., Comptonized emission). In the case of GX 340+0, we find a similar PA in HB and NB, which would support this assumption and motivate simulations with different geometrical parameters to explain the observations. We note that the spectral parameters used in the simulations by A. Gnarini et al. (2022) are significantly different from the parameter estimates from the spectral modeling. However, at present, these are the best cases for comparison.

Alternatively, the polarized emission can also arise from a broad SL. However, the emission from SL is expected to have a strong variation of PA as a function of the energy and the expected PD of the SL would be typically 1.5% or lower (A. Bobrikova et al. 2025) and since our observations have shown constant PA as a function of the energy (at least greater than 3 keV for both the HB and NB), and a higher PD in HB we can rule out SL as a possible origin for polarized emission. Another possibility is that the polarized emission arises from the reflection component. F. La Monaca et al. (2024a) have explored this for the HB observation of GX 340+0 and suggested that it is difficult to disentangle whether the observed PD arises solely from the reflection component or solely from Comptonized emission.

### *4.2. Radio Emission from GX 340+0 and Its Correlation with the X-Rays*

During the first GMRT observation on 2024 August 12, GX 340+0 was in the NB. No radio emission was detected at 700 MHz, with a $3\sigma$ upper limit of 1.1 mJy. During the second GMRT observation 2 days later (on 2024 August 14), GX 340+0 had transitioned to the HB branch, and the 1.26 GHz observations tentatively detected GX 340+0 with a flux density of 4.5 ± 0.7 mJy. At the start of the ATCA observations the next day (2024 August 15), the target was initially within the FB, transitioning back to the NB during the observation (Figure 1). The ATCA observations detected radio emission from GX 340+0 with a flux density of 0.70 ± 0.05 mJy at 5.5 GHz and 0.59 ± 0.05 mJy at 9 GHz. The measured flux densities could be consistent with emission from both a compact or transient jet, where the errors in the radio spectrum do not allow us to discriminate between the two. However, imaging the source on shorter timescales suggests that the radio emission was found to be fading at both frequencies during the first half of the ATCA observation (by a factor of 2–3) before remaining steady for the second half. Z-sources typically display fading radio emission as the source moves from the HB to the FB, with radio flares detected around the transition between the NB and HB, indicating the launching of ejecta (e.g., R. Fender et al. 2004a; S. E. Motta & R. P. Fender 2019). Our results fit into this picture, where ejecta are expected to be launched over the HB → NB transition, which then fades as the source moves toward the FB. We propose that the ATCA observations detected the fading of the flaring associated with this transition, before stabilizing as the source started to move back from the FB to the NB (when we expect it to begin to brighten; e.g., C. F. Bradshaw et al. 2003; S. Migliari et al. 2007; M. Bałucińska-Church et al. 2010; M. J. Church et al. 2012).

The results from the GMRT observations also fit the general picture of radio behavior of Z-sources; the nondetection during NB occurs due to a spectral turnover of the synchrotron emission at >700 MHz, likely arising from free–free or synchrotron self-absorption (see discussions in Paper I). Z-sources are at their radio brightest during the HB, where the emission likely arises from a steady jet (e.g., S. Migliari et al. 2007). As such, the tentative detection at 1.26 GHz on 2024 August 15 as the source moves along the HB could be radio emission from a bright, steady jet.

## 5. Conclusions

Based on an extensive campaign of GX 340+0 in X-ray and radio wavelengths during its evolution along its Z-track, we constrained the spectral and polarimetric properties of the source within the NB. Here, we summarize some of the key properties of the source we have inferred from the analysis:

1. We estimated the broadband polarization (2–8 keV) of GX 340+0 during the NB at 1.3% ± 0.3% with a PA of 38° ± 6°.
2. The spectral analysis of the source using various instruments suggested the presence of three continuum components in the spectra: a low-temperature accretion disk, a hot blackbody component (perhaps from the surface), and a Comptonized emission, as well as a Gaussian emission component corresponding to reprocessed emission from the accretion disk.
3. Spectro-polarimetric study of the observations suggests that the PD of the Comptonizing medium in NB is weaker than that in HB.
4. The X-ray polarization was significantly detected at energies >3.2 keV and the PA of the source is similar in NB and HB, suggesting a similar origin of the polarized emission in the source in both branches, perhaps from the Comptonizing medium. The additional component, whose presence is hinted at in HB, apparently does not emit strongly in the NB.

## Acknowledgments

The Imaging X-ray Polarimetry Explorer (IXPE) is a joint US and Italian mission. The US contribution is supported by the National Aeronautics and Space Administration (NASA) and led and managed by its Marshall Space Flight Center (MSFC), with industry partner Ball Aerospace (now, BAE Systems). The Italian contribution is supported by the Italian Space Agency (Agenzia Spaziale Italiana, ASI) through contract ASI-OHBI-2022-13-I.0, agreements ASI-INAF-2022-19-HH.0 and

ASI-INFN-2017.13-H0, and its Space Science Data Center (SSDC) with agreements ASI-INAF-2022-14-HH.0 and ASI-INFN 2021-43-HH.0, and by the Istituto Nazionale di Astrofisica (INAF) and the Istituto Nazionale di Fisica Nucleare (INFN) in Italy. This research used data products provided by the IXPE Team (MSFC, SSDC, INAF, and INFN) and distributed with additional software tools by the High-Energy Astrophysics Science Archive Research Center (HEASARC), at NASA Goddard Space Flight Center (GSFC). This work makes use of data from the AstroSat mission of the Indian Space Research Organisation (ISRO), archived at the Indian Space Science Data Centre (ISSDC). The article has used data from the SXT and the LAXPC developed at TIFR, Mumbai, and the AstroSat POCs at TIFR are thanked for verifying and releasing the data via the ISSDC data archive and providing the necessary software tools. This work was supported by NASA through the NICER mission and the Astrophysics Explorers Program. This work has made use of the data from the Insight-HXMT mission, a project funded by the China National Space Administration (CNSA) and the Chinese Academy of Sciences (CAS).

This research has also made use of data and/or software provided by the High Energy Astrophysics Science Archive Research Center (HEASARC), which is a service of the Astrophysics Science Division at NASA/GSFC and the High Energy Astrophysics Division of the Smithsonian Astrophysical Observatory. We thank the staff of the GMRT who made these observations possible. GMRT is run by the National Centre for Radio Astrophysics of the Tata Institute of Fundamental Research. The Australia Telescope Compact Array is part of the Australia Telescope National Facility (https://ror.org/05qajvd42), which is funded by the Australian Government for operation as a National Facility managed by CSIRO. We acknowledge the Gomeroi people as the Traditional Owners of the ATCA observatory site. We thank Jamie Stevens and the ATCA staff for making the observations possible. Y.B. and A.B. would like to especially thank Dr. Shriharsh Tendulkar for valuable discussion on radio observations and insights into the emission from the NSs. T.D.R. is an IAF research fellow. M.N. is a Fonds de Recherche du Quebec - Nature et Technologies (FRQNT) postdoctoral fellow. L.Z. acknowledges support from the National Natural Science Foundation of China (NSFC) under grant 12203052. J.H. acknowledges support for this work from the IXPE Guest Investigator program under NASA grant 80NSSC24K1746.

*Facilities:* IXPE, AstroSat, NICER, Insight-HXMT, GMRT, ATCA.

*Software:* `astropy` (Astropy Collaboration et al. 2018), `ixpeobssim` (L. Baldini et al. 2022), `CASA` (CASA Team et al. 2022), `Stingray` (D. Huppenkothen et al. 2019a, 2019b).

## Appendix
## Effect of Softer Color Definition on the HID

We note that the FB and the EFB are not identifiable in the HID created using the soft X-ray bands (i.e., using the HR from any subset of energy bands in 3–10 keV; see Figure 2). We construct the HID from the AstroSat-LAXPC observation in the energy bands used for NICER, i.e., 3–10 keV for the count rate and HR between the 5–10 and 3–5 keV bands (shown in Figure 5). We observe that a single track similar to the NB is visible in the HID. The points corresponding to the FB and the EFB are identified from Figure 2 and marked as black circles in Figure 5. Additionally, the AstroSat observation shows a significant overlap with the NICER observation during one of the FB excursions. The light curves from both observations seem to indicate the presence of a flare (during the FB), but the HR between the 5–10 and 3–5 keV bands was similar for both the FB and NB. Therefore, it is challenging to accurately identify any FB intervals solely based on data from the soft X-ray instruments used here (i.e., NICER or IXPE).

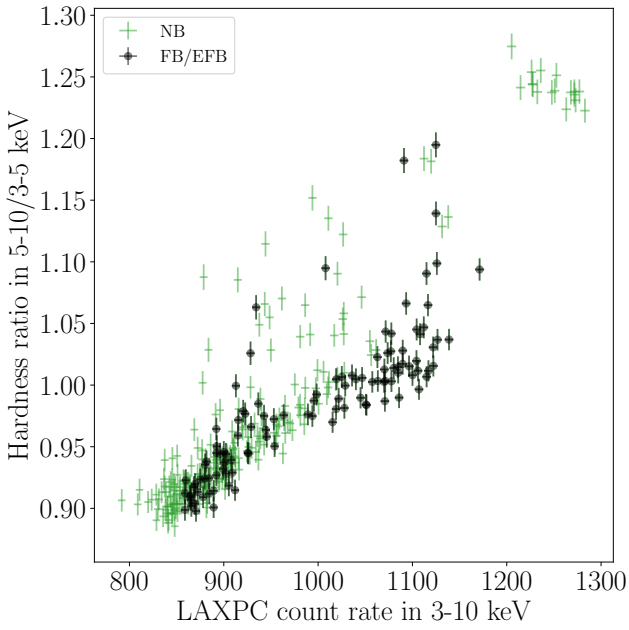


**Figure 5.** HID of GX 340+0 as seen by AstroSat-LAXPC in the soft energy range. To highlight the overlap of the FB/EFB and the NB in the soft energy range, we depict the FB/EFB (as seen in Figure 2) as black circles while the green points correspond to the NB and hard apex. A definition using soft X-rays of the HR is unable to differentiate between the NB and the FB, indicating that the distinctive shape of the FB/EFB is mainly due to changes in the 10–20 keV count rate.

## ORCID iDs

Yash Bhargava https://orcid.org/0000-0002-5967-8399
Thomas D. Russell https://orcid.org/0000-0002-7930-2276
Mason Ng https://orcid.org/0000-0002-0940-6563
Arvind Balasubramanian https://orcid.org/0000-0003-0477-7645
Liang Zhang https://orcid.org/0000-0003-4498-9925
Swati Ravi https://orcid.org/0000-0002-2381-4184
Vishal Jadoliya https://orcid.org/0009-0005-0366-0834
Sudip Bhattacharyya https://orcid.org/0000-0002-6351-5808
Mayukh Pahari https://orcid.org/0000-0002-5900-9785
Jeroen Homan https://orcid.org/0000-0001-8371-2713
Herman L. Marshall https://orcid.org/0000-0002-6492-1293
Deepto Chakrabarty https://orcid.org/0000-0001-8804-8946
Francesco Carotenuto https://orcid.org/0000-0002-0426-3276
Aman Kaushik https://orcid.org/0009-0005-6441-0468

## References

Antia, H. M., Agrawal, P. C., Dedhia, D., et al. 2021, JApA, 42, 32
Astropy Collaboration, Price-Whelan, A. M., Sipőcz, B. M., et al. 2018, AJ, 156, 123
Baldini, L., Bucciantini, N., Lalla, N. D., et al. 2022, SoftX, 19, 101194
Bałucińska-Church, M., Gibiec, A., Jackson, N. K., & Church, M. J. 2010, A&A, 512, A9

Berendsen, S. G. H., Fender, R., Kuulkers, E., Heise, J., & van der Klis, M. 2000, MNRAS, 318, 599
Bhargava, Y., Bhattacharyya, S., Homan, J., & Pahari, M. 2023, ApJ, 955, 102
Bhargava, Y., Ng, M., Zhang, L., et al. 2024, arXiv:2405.19324
Bobrikova, A., Poutanen, J., & Loktev, V. 2025, A&A, 696, A181
Bradshaw, C. F., Geldzahler, B. J., & Fomalont, E. B. 2003, ApJ, 592, 486
CASA Team, Bean, B., Bhatnagar, S., et al. 2022, PASP, 134, 114501
Chakraborty, M., Bhattacharyya, S., & Mukherjee, A. 2011, MNRAS, 418, 490
Chen, Y. P., Zhang, S., Qu, J. L., et al. 2018, ApJL, 864, L30
Church, M. J., Dimbylow, O., Peach, C., & Balucinska-Church, M. 2010, MmSAI, 81, 275
Church, M. J., Gibiec, A., Bałucińska-Church, M., & Jackson, N. K. 2012, A&A, 546, A35
Church, M. J., Halai, G. S., & Bałucińska-Church, M. 2006, A&A, 460, 233
Cocchi, M., Gnarini, A., Fabiani, S., et al. 2023, A&A, 674, L10
Di Marco, A., Fabiani, S., La Monaca, F., et al. 2022, AJ, 164, 103
Di Marco, A., Soffitta, P., Costa, E., et al. 2023, AJ, 165, 143
Fabiani, S., Capitanio, F., Iaria, R., et al. 2024, A&A, 684, A137
Farinelli, R., Fabiani, S., Poutanen, J., et al. 2023, MNRAS, 519, 3681
Fender, R., Wu, K., Johnston, H., et al. 2004a, Natur, 427, 222
Fender, R. P., Belloni, T. M., & Gallo, E. 2004b, MNRAS, 355, 1105
Fomalont, E. B., Geldzahler, B. J., & Bradshaw, C. F. 2001a, ApJL, 553, L27
Fomalont, E. B., Geldzahler, B. J., & Bradshaw, C. F. 2001b, ApJ, 558, 283
Forsblom, S. V., Tsygankov, S. S., Poutanen, J., et al. 2024, A&A, 691, A216
Fridriksson, J. K., Homan, J., & Remillard, R. A. 2015, ApJ, 809, 52
Gendreau, K. C., Arzoumanian, Z., Adkins, P. W., et al. 2016, SPIE, 9905, 99051H
Gibiec, A., Balucinska-Church, M., & Church, M. 2011, in The X-ray Universe 2011, ed. J.-U. Ness & M. Ehle, 212
Gnarini, A., Ursini, F., Matt, G., et al. 2022, MNRAS, 514, 2561
Hasinger, G., & van der Klis, M. 1989, A&A, 225, 79
HI4PI Collaboration, Ben Bekhti, N., Flöer, L., et al. 2016, A&A, 594, A116
Hjellming, R. M., Han, X. H., Cordova, F. A., & Hasinger, G. 1990a, A&A, 235, 147
Hjellming, R. M., Stewart, R. T., White, G. L., et al. 1990b, ApJ, 365, 681
Homan, J., van der Klis, M., Fridriksson, J. K., et al. 2010, ApJ, 719, 201
Homan, J., van der Klis, M., Wijnands, R., et al. 2007, ApJ, 656, 420
Huppenkothen, D., Bachetti, M., Stevens, A., et al. 2019a, JOSS, 4, 1393
Huppenkothen, D., Bachetti, M., Stevens, A. L., et al. 2019b, ApJ, 881, 39
Iaria, R., Lavagetto, G., Di Salvo, T., et al. 2006, ChJAS, 6, 257
Inogamov, N. A., & Sunyaev, R. A. 1999, AstL, 25, 269
Jonker, P. G., van der Klis, M., Wijnands, R., et al. 2000, ApJ, 537, 374
Kaastra, J. S., & Bleeker, J. A. M. 2016, A&A, 587, A151
Kaddouh, M. A., Sudha, M., & Ludlam, R. M. 2024, RNAAS, 8, 243
Kale, R., & Ishwara-Chandra, C. H. 2021, ExA, 51, 95
Kislat, F., Clark, B., Beilicke, M., & Krawczynski, H. 2015, APh, 68, 45
La Monaca, F., Di Marco, A., Ludlam, R. M., et al. 2024a, A&A, 691, A253
La Monaca, F., Di Marco, A., Poutanen, J., et al. 2024b, ApJL, 960, L11
Lapidus, I. I., & Sunyaev, R. A. 1985, MNRAS, 217, 291
Li, L.-X., Narayan, R., & McClintock, J. E. 2009, ApJ, 691, 847
Lin, D., Remillard, R. A., & Homan, J. 2009, ApJ, 696, 1257
Lin, D., Remillard, R. A., Homan, J., & Barret, D. 2012, ApJ, 756, 34
Markwardt, C., Arzoumanian, Z., Gendreau, K., Hare, J., & Team, N. 2024, AAS/HEAD, 21, 105.36
Migliari, S., & Fender, R. P. 2006, MNRAS, 366, 79
Migliari, S., Miller-Jones, J. C. A., Fender, R. P., et al. 2007, ApJ, 671, 706
Miller, B. W., Margon, B., & Burton, M. G. 1993, AJ, 106, 28
Miller, J. M., Raymond, J., Cackett, E., Grinberg, V., & Nowak, M. 2016, ApJL, 822, L18
Misra, R., Roy, J., & Yadav, J. S. 2021, JApA, 42, 55
Mitsuda, K., Inoue, H., Nakamura, N., & Tanaka, Y. 1989, PASJ, 41, 97
Motta, S. E., & Fender, R. P. 2019, MNRAS, 483, 3686
Ng, M., Hughes, A. K., Homan, J., et al. 2024, ApJ, 966, 232
Oosterbroek, T., Lewin, W. H. G., van Paradijs, J., et al. 1994, A&A, 281, 803
Penninx, W., Zwarthoed, G. A. A., van Paradijs, J., et al. 1993, A&A, 267, 92
Priedhorsky, W., Hasinger, G., Lewin, W. H. G., et al. 1986, ApJL, 306, L91
Rankin, J., La Monaca, F., Di Marco, A., et al. 2024, ApJL, 961, L8
Seifina, E., Titarchuk, L., & Frontera, F. 2013, ApJ, 766, 63
Shakura, N. I., & Sunyaev, R. A. 1988, AdSpR, 8, 135
Singh, K. P., Tandon, S. N., Agrawal, P. C., et al. 2014, SPIE, 9144, 91441S
Smale, A. P., Homan, J., & Kuulkers, E. 2003, ApJ, 590, 1035
Sriram, K., Rao, A. R., & Choi, C. S. 2011, ApJL, 743, L31
van der Klis, M. 2004, arXiv:0410551
Verner, D. A., Ferland, G. J., Korista, K. T., & Yakovlev, D. G. 1996, ApJ, 465, 487
White, N. E., Stella, L., & Parmar, A. N. 1988, ApJ, 324, 363
Wilms, J., Allen, A., & McCray, R. 2000, ApJ, 542, 914
Yadav, J. S., Agrawal, P. C., Antia, H. M., et al. 2016, SPIE, 9905, 99051D
Yadav, J. S., Agrawal, P. C., Antia, H. M., et al. 2017, CSci, 113, 591
Zdziarski, A. A., Johnson, W. N., & Magdziarz, P. 1996, MNRAS, 283, 193
Zhang, S.-N., Li, T., Lu, F., et al. 2020, SCPMA, 63, 249502
Życki, P. T., Done, C., & Smith, D. A. 1999, MNRAS, 309, 561